Received: 23 January 2017 | Revised: 13 March 2017 | Accepted: 14 March 2017

DOI: 10.1002/nbm.3729

WILEY NMR IN BIOMEDICINE

REVIEW ARTICLE

Electric properties tomography: Biochemical, physical and technical background, evaluation and clinical applications

Ulrich Katscher[1] | Cornelius A.T. van den Berg[2]

[1] Department of Tomographic Imaging, Philips Research Laboratories, Hamburg, Germany

[2] Department of Radiotherapy, University Medical Center, Utrecht, the Netherlands

Correspondence
U. Katscher, Department of Tomographic Imaging, Philips Research Laboratories, Roentgenstrasse 24–26, 22335 Hamburg, Germany.
Email: ulrich.katscher@philips.com

Electric properties tomography (EPT) derives the patient's electric properties, i.e. conductivity and permittivity, using standard magnetic resonance (MR) systems and standard MR sequences. Thus, EPT does not apply externally mounted electrodes, currents or radiofrequency (RF) probes, as is the case in competing techniques. EPT is quantitative MR, i.e. it yields absolute values of conductivity and permittivity. This review summarizes the physical equations underlying EPT, the corresponding basic and advanced reconstruction techniques and practical numerical aspects to realize these reconstruction techniques. MR sequences which map the field information required for EPT are outlined, and experiments to validate EPT in phantom and *in vivo* studies are described. Furthermore, the review describes the clinical findings which have been obtained with EPT so far, and attempts to understand the physiologic background of these findings.

KEYWORDS

electric conductivity, EPT, numerical differentiation, permittivity, tumor characterization

1 | INTRODUCTION

The contrast of standard magnetic resonance (MR) images is determined by a non-trivial weighting of numerous local physiologic parameters. From the early beginnings, magnetic resonance imaging (MRI) aimed to extract these physiologic parameters quantitatively from the original magnetization-weighted images. The resulting parameter maps allow a more direct access to clinical diagnosis, as well as increased comparability between different examinations, different patients and different hospitals. Although it has been known for decades how to extract many of these physiologic parameters, the trend towards the extraction of further parameters is still ongoing. Most recent examples of this trend are electromagnetic (EM) tissue parameters. In the past 5–10 years, methods have been demonstrated for extracting the magnetic susceptibility from MR images (see, for example, recent reviews[1,2]). More or less in the same time frame, it has been extraction of electrical properties (EPs, i.e. conductivity and permittivity) from MR images has also been extracted.

Before MRI, electrical tissue properties could be obtained non-invasively by the technique of electrical impedance tomography (EIT) via the injection of external currents into the patient, measuring the tissue impedance between multiple points of the patient's surface (for a review, see Holder[3]). With the development of MRI, MRI was combined with the EIT technique of injecting external currents, thus combining the ability of EIT to probe EPs with the high spatial resolution of MRI. This combination was first realized as MR-current density imaging (MR-CDI) using DC,[4,5] and the corresponding radiofrequency-current density imaging (RF-CDI).[6-8] From the current density obtained, the corresponding conductivity can be derived, yielding the separate area of MR-EIT (see, for instance, previous studies[9-11]). Although EIT is an ill-posed problem, because the applied surface electrodes monitor only the scatter field at a distance from the region of interest (ROI), MR-EIT greatly improves inversion conditions by converting the problem into a so-called hybrid inversion problem because of its ability to map the magnetic field throughout the ROI.

The currents required to image EPs do not necessarily have to be injected by external electrodes as in EIT described above. Alternatively, eddy currents can be induced by the application of magnetic RF fields,

Abbreviations used: APT, amide proton transfer; CDI, current density imaging; CSI, contrast source inversion; DWI, diffusion-weighted imaging; EIT, electrical impedance tomography; EM, electromagnetic; EMF, electromagnetic field; EP, electric property; EPT, electric properties tomography; FET, fluoro-ethyl-tyrosine; FLAIR, fluid-attenuated inversion recovery; gEPT, gradient-based electric properties tomography; LMT, local Maxwell tomography; MPRAGE, magnetization-prepared rapid gradient echo; MR, magnetic resonance; MRI, magnetic resonance imaging; MS, multiple sclerosis; PET, positron emission tomography; PR, progesterone receptor; QBC, quadrature body coil; QSM, quantitative susceptibility mapping; RF, radiofrequency; ROI, region of interest; RX, receive; SAEP, single acquisition electrical properties; SAR, specific absorption rate; SNR, signal-to-noise ratio; SSFP, steady-state free precession; TX, transmit; UTE, ultrashort TE; wEPT, water content-based electric properties tomography; WHO, World Health Organization; ZTE, zero TE

avoiding the sensation of pain frequently connected with external current injection. As magnetic RF fields at Larmor frequency (i.e. typically around 100 MHz) are an inherent component of MRI, the desired currents can be created by standard MR systems and standard MR sequences. The resulting imaging technique, called electrical properties tomography (EPT or MR-EPT),[12-14] is the subject of this review.

The basic idea of EPT is that the conductivity and permittivity of the patient distort B_1, the component of the magnetic RF field responsible for spin excitation. Measurements of this distorted B_1 field distribution (see, for example, previous studies[15-18] for B_1 magnitude mapping, and the discussion of B_1 phase mapping below) allows the reconstruction of the EPs causing the observed distortions. The B_1 mapping techniques are typically applied to obtain a starting point for compensation of these distortions. In contrast, EPT appreciates the distortions as access to the desired electrical tissue parameters.

Without calling the approach EPT, the first mention of EPT was in the early 1990s by Haacke et al.[12] However, these workers did not pursue EPT further because of 'spurious phase effects unrelated to RF penetration which make a simple extraction difficult' (i.e. phase effects predominantly belonging to imperfections of the MR systems back in the early 1990s). Instead of the mentioned 'simple extraction' of the EPs, Haacke et al[12] developed a heterogeneous layer model as workaround for the observed spurious phase effects. The first successful application of EPT (still not called EPT) is dated more than 10 years after the initial article of Haacke et al[12] in a conference abstract by Wen.[13] In principle, this abstract described the pathway to clinically feasible EPT. However, after this publication, Wen left the topic of EPT, and again EPT was not pursued further for years.

Systematic research on EPT started in 2009,[14] based on the same concepts as proposed earlier by Haacke et al[12] and Wen.[13] It additionally applied EPT to estimate the local specific absorption rate (SAR) by discerning not only EPs, but also electric fields from MR measurements.

Since 2009, research on EPT has widened, and more and more groups have started to investigate different aspects of EPT, yielding the focus of this review.

As mentioned previously, EPT is based on eddy currents induced by magnetic RF fields. The resulting EPs, which generally depend on the applied frequency, belong to the MHz range corresponding to the Larmor frequency of the current main field strength. Eddy currents in the tissue can also be induced by gradient switching, corresponding to a much lower frequency in the range of kHz, as is the case for the above-mentioned MR-EIT. Discussions are ongoing as to whether these eddy currents enable a 'low-frequency' EPT in contrast with the above-described 'RF'-EPT.[19-26] As recent results have indicated that these currents are too weak for MR detection, low-frequency EPT is not considered further in this review.

This review is organized as follows. The theory of EPT is divided into two parts. The first part presents the physical equations underlying EPT and the basic reconstruction techniques resulting directly from these physical equations. The second part describes the reconstruction techniques of a 'second generation', which are particularly designed to cope with the specific issues of EPT. The following two sections can be considered as 'Methods' sections: first, 'Numerics' outlines practical aspects to realize the aforementioned reconstruction techniques; second, MR sequences are outlined which map the field information required for EPT. The section 'Validation experiments' is dedicated to phantom and *in vivo* studies conducted to evaluate EPT. Finally, the section 'Physiologic background of electrical tissue properties' attempts to biochemically understand the clinical findings which have been obtained with EPT so far and which are described in the last section.

2 | BASIC RECONSTRUCTION TECHNIQUES

The complex permittivity, which is assumed to be isotropic, $\kappa = \omega\varepsilon - i\sigma$, at an angular frequency ω can be related to the time-harmonic, source-free magnetic field $\mathbf{H}$ by the following combination of Faraday's and Ampere's law (so-called Helmholtz equation):

$$-\Delta\mathbf{H} = \mu\omega\kappa\mathbf{H} + \frac{\nabla\kappa}{\kappa}\times[\nabla\times\mathbf{H}] \tag{1}$$

The magnetic permeability μ (at RF operating frequency) is assumed to be constant, and thus is replaced by the magnetic vacuum permeability μ_0 hereafter. The Helmholtz equation (Equation 1) does not depend on the particular scaling of $\mathbf{H}$. In particular, without introducing significant changes, $\mathbf{H}$ might be scaled with the (as mentioned, assumed to be constant) μ, i.e. Equation 1 could also be based on the magnetic flux density $\mathbf{B}$, which is typically used in connection with MR RF fields. The second term on the right-hand side of Equation 1 describes spatially varying κ and can be neglected in areas in which κ is (nearly) constant:

$$\nabla\kappa \approx 0 \tag{2}$$

Neglecting this term yields:

$$-\Delta\mathbf{H} = \mu_0\omega\kappa\mathbf{H} \tag{3}$$

and has the advantage that mutual coupling of different spatial components of $\mathbf{H}$ is removed: the 'truncated' Helmholtz equation (Equation 3) is valid for each component of $\mathbf{H}$ separately, which can be easily solved for the unknown κ. Of particular interest is Equation 3 for the positive circularly polarized component $H^+ = (H_x + iH_y)/2$ corresponding to the RF excitation of MRI:

$$\kappa = \frac{-\Delta H^+}{\mu_0\omega H^+} \tag{4}$$

The scaling of H^+ cancels in the nominator and denominator of Equation 4, yielding absolute values of κ even for unknown scaling of H^+.

To solve Equation 4, both the magnitude and phase of H^+ are required. Unfortunately, only the magnitude of H^+ can be measured exactly (via 'B_1 mapping', see section 5). The phase of H^+, usually called φ^+, is difficult to determine exactly. The phase of a standard MR image is always the superposition of φ^+ with its counterpart from RF reception, φ^- of H^-, and thus is called the transceive phase: $\varphi_0 = \varphi^+ + \varphi^-$.[27] In a standard MR system with a quadrature body coil (QBC), the sign of the circular polarization of this coil is switched from RF transmission to RF reception for the sake of optimizing the signal-to-noise ratio (SNR). The resulting $\widetilde{\varphi}^-$ of the switched QBC closely resembles φ^+,[13,14] leading to the approximation of φ^+ by:

$$\varphi^+ \approx \varphi_0/2 = (\varphi^+ + \widetilde{\varphi}^-)/2 \tag{5}$$

sometimes called the 'transceive phase assumption'. This assumption is, strictly speaking, only accurate for transverse symmetrical objects

placed in the center of quadrature volume coils, providing a perfectly circularly polarized transmit (TX) and receive (RX) field.[28] For objects such as the brain, with deviations from this perfect circular polarization (i.e. with elliptic contributions), the validity will deteriorate, but is still applicable for field strengths up to 3 T.[29] For higher field strengths, where the transverse dimensions approach the 'optical' wavelength, significant errors arise in peripheral brain regions.[29]

A further simplification of EPT is obtained by separating the real and imaginary parts of Equation 4, i.e. calculating the conductivity via:

$$\sigma = \frac{1}{\mu_0\omega}\,\mathrm{Im}\left\{\frac{\Delta H^+}{H^+}\right\} = (\mu_0\omega)^{-1}\left(\Delta\varphi^+ + \nabla\ln\left(|H^+|\right)\cdot\nabla\varphi^+\right) \tag{6}$$

and the permittivity via:

$$\varepsilon = -\frac{1}{\mu_0\omega^2}\,\mathrm{Re}\left\{\frac{\Delta H^+}{H^+}\right\} = \left(\mu_0\omega^2\right)^{-1}\left[-\frac{\Delta|H^+|}{|H^+|} + \left(\nabla\varphi^+\right)^2\right] \tag{7}$$

To the leading order, the conductivity is reflected by the curvature in the phase of the RF field, whereas the permittivity is reflected by the curvature in the magnitude of the RF field. It has been shown[30,31] that the magnitude-related term $\nabla\ln(|H^+|)\cdot\nabla\varphi^+$ in Equation 6 and the phase-related term $(\nabla\varphi^+)^2$ in Equation 7 are only of the order of 10–20% of the leading terms for typical κ of human tissue at 1.5 or 3 T. Thus, σ can be estimated by 'phase-based EPT':

$$\sigma \approx \frac{\Delta\varphi^+}{\mu_0\omega} \tag{8}$$

(i.e. Poisson's equation), and ε can be estimated by 'magnitude-based EPT':

$$\varepsilon \approx -\frac{\Delta|H^+|}{\mu_0\omega^2|H^+|} \tag{9}$$

which could be regarded as the 'normalized' Poisson's equation. If only permittivity or only conductivity is required for diagnosis, it might be sufficient to measure only the magnitude or phase of B_1, thus shortening the required MR scanning. In particular, skipping the mapping of the magnitude of B_1, which is typically a rather lengthy scan, significantly speeds up the scan time required for EPT, even enabling real-time conductivity measurements.[32]

The linearity of phase-based EPT (Equation 8) supersedes the QBC transceive phase assumption (Equation 5), allowing arbitrary combinations of RF TX and RX coils. The resulting transceive phase, containing φ^+ and φ^- from different RF fields, still yields σ via:

$$\sigma = \frac{\Delta(\varphi_0/2)}{\mu_0\omega} = \frac{\Delta(\varphi^+ + \varphi^-)}{2\mu_0\omega} = \frac{\Delta\varphi^+/(\mu_0\omega) + \Delta\varphi^-/(\mu_0\omega)}{2} = \frac{2\sigma}{2} = \sigma \tag{10}$$

as Equation 8 can be based on φ^+, φ^- or any phase fulfilling Maxwell's equations, leading to the same σ as long as the magnitude related to this phase is ('sufficiently') constant.

Various studies have reported severe artifacts along tissue boundaries in the form of strong oscillations (undershooting/overshooting; see, for example, previous studies[14,33,34]). Traditionally, these artifacts are assigned to the violation of the assumption of the locally constant κ. However, an additional contribution arises from the numerical implementation of the calculus operations of the EPT equation applied, which always involves a number of voxels in the neighborhood of the target voxel to be reconstructed. This so-called kernel of involved voxels contributes to the mentioned oscillations as soon as it contains B_1 field data of voxels of different κ. Thus, the boundary issue comprises two aspects: a physical aspect by violating the assumption given by Equation 2, and a numerical aspect by the difficulty of accurately differentiating where fields have discontinuous derivatives.

This boundary issue, as well as the transceive phase issue described above, has given rise to research into advanced EPT reconstruction methods which overcome these issues, as described in the following.

3 | ADVANCED RECONSTRUCTION TECHNIQUES

An advanced reconstruction framework for EPT, called gradient-based electrical properties tomography (gEPT), was described by Liu et al.[35] It is based on the full Helmholtz equation, thus including gradients in EPs at tissue boundaries. Assuming that derivatives of H_z are much smaller than derivatives of $H^\pm$, which is generally true for most coil types in the central imaging zone, these authors demonstrated that all three spatial EP gradients could be reconstructed from multi-channel transceiver H^+ or H^- field data. By subsequent spatial integration starting from certain seed points with known EP, the complete EP distribution can be recovered. The authors claim that this integration acts as a low-pass filter and thus provides robustness towards noise on field data. The gEPT framework is free of any phase assumptions and its performance has been shown for the human brain at 7 T using a microstrip transceiver array.

The full Helmholtz equation was also exploited for reconstruction by Hafalir et al.[36] Here, the equation was transformed to a partial differential equation forming a convection–reaction–diffusion equation in contrast with Liu et al,[35] but again assuming that derivatives of H_z are much smaller than derivatives of $H^\pm$. Later, this convection–reaction type of reconstruction was extended to take only the transceive phase φ_0 as input,[37] similar to the initially proposed phase-based EPT.[30,31] The final reconstruction requires solution of the equation (with resistivity $\rho = 1/\sigma$):

$$-c\nabla^2\rho + (\nabla\varphi_0\cdot\nabla\rho) + \nabla^2\varphi_0\cdot\rho - 2\mu_0\omega = 0 \tag{11}$$

which can be discretized and solved with a finite difference scheme. The first term in Equation 11 is a diffusion term where c is a constant diffusion coefficient. This term does not appear in the EM derivation, but is added 'artificially' to stabilize the solution and suppress spurious oscillations. It acts as a low-pass filter, leading to some blurring of the final conductivity maps. In addition to neglecting derivatives of H_z, the derivation of Equation 11 is based on two assumptions: (i) $|\nabla H_1^+| \approx |\nabla H_1^-| \approx 0$; and (ii) $\sigma >> \omega\varepsilon$. These assumptions also underlie the 'phase-based conductivity imaging' equation (Equation 8), which results from Equation 11 for $\nabla\rho = 0$. As pointed out above, assumptions (i) and (ii) lead to overestimations of conductivity (e.g. approximately 20% for white and gray matter at 3 T).

As mentioned previously, the RF transmission as well as the reception process contribute to the image phase, and these two contributions are usually separated via the 'transceive phase assumption' (see Wen[13] and Katscher et al,[14] and Equation 5) applicable for quadrature (i.e. body or head) coils. To address this phase issue, various studies have explored alternative approaches compatible with more general TX arrays. An approach based on Gauss' law was published by Zhang et al,[38] assuming gradients in H_z to be negligible. A more general methodology exploits the fact that the EPT reconstructions based on H^+ fields of various TX channels should result in equal EPs. This central concept was first introduced by the 'dual excitation algorithm',[39] where it was applied to the EPT boundary problem. Later,[40,41] this concept was explored to isolate the RX phase (common for all TX channels) and thus to obtain absolute H^+ phase maps for all TX channels. The approach presented by Marques et al[42] differentiates itself by reconstructing EP maps based solely on relative sensitivity maps of RX coils. This has the advantage that (in contrast with map TX coil sensitivities) all coil sensitivities can be mapped simultaneously in a fast single scan, and thus the method was dubbed 'single acquisition electrical properties mapping' (SAEP mapping). A more generalized methodology was presented by Sodickson et al,[43,44] which aimed to reconstruct even more EM quantities by considering the general case of anisotropy and gradient in EPs, called (generalized) 'local Maxwell tomography' (LMT). All of these methodologies face, in practice, a major challenge. They solve matrix vector equations constructed of local first- and second-order (for SAEP, even third-order) field derivatives, albeit with differing numbers of unknowns. This requires H^+ magnitude and phase maps with minimal noise levels, which are, in practice, not very realistic. In addition, some of the inversions of the various approaches are ill-posed.

3.1 | Forward based EPT

The aforementioned methodologies can be categorized as 'direct' methods, as EPs are calculated directly from the measured B_1 field. In another view, this direct calculation is running 'backwards' from the measured B_1 field to the underlying EPs. An alternative approach, as proposed by various studies,[45-48] is a general inverse method, running 'forwards' from tissue EPs to (measurable and non-measurable) fields. Thus, this approach fits a model of the EP distribution to the B_1 field avoiding any differentiation on the measured B_1 field. The fitting takes places by iterative minimization of a large system (over all voxels) of non-linear equations with iterative methods, such as conjugate gradient methods. An additional advantage is that, in addition to data fidelity terms, data consistency terms can be included in the objective function[45] or even regularization terms minimizing, for instance, total variation.[45-47] A downside is, of course, the increased computational costs and potential issues concerning local minima. In the remainder of this section, one of these inverse EPT approaches [so-called contrast source inversion-EPT (CSI-EPT)[45]] is reviewed in more detail.

The reconstruction framework of CSI-EPT comprises two equations: the so-called 'data equation' and 'object equation', including magnetic and electric field information, respectively. Given the known background field H^+_{bg} of the empty RF coil, the scattered field $H^+_{scatter} = H^+ - H^+_{bg}$ is related to the contrast source $\mathbf{w}(\mathbf{r}) = \chi(\mathbf{r})\mathbf{E}(\mathbf{r})$, where $\mathbf{E}(\mathbf{r})$ is the electric field. The contrast function $\chi(\mathbf{r}) = \kappa(\mathbf{r})/\kappa_{bg} - 1$ is linked to the permittivity and conductivity of the object $\kappa(\mathbf{r})$ and the background κ_{bg}. This relationship between $H^+_{scatter}$ and $\mathbf{w}$ is described by the 'data equation':

$$F_{data}(\mathbf{w}(\mathbf{r})) = H^+_{scatter} - \frac{1}{2}\left(\int_V G_1^{HJ}(\mathbf{r},\mathbf{r}') + i\cdot G_2^{HJ}(\mathbf{r},\mathbf{r}')\right)\cdot\mathbf{w}(\mathbf{r}')\cdot dV = 0 \quad (12)$$

where G^{HJ} is the 'electric current to magnetic field' Green's tensor. The integration in Equation 12 is performed over the whole volume of the scattered medium (denoted by $\mathbf{r}'$). Subsequently, the 'object equation' is formed, relating each spatial Cartesian component k of the background and total electric field, $\mathbf{E}_k^{bg}$ and $\mathbf{E}_k$, respectively:

$$F_{object}(\mathbf{w}(\mathbf{r}),\chi(\mathbf{r})) = \chi(\mathbf{r})E_k(\mathbf{r}) - \chi(\mathbf{r})\int_V G_k^{EJ}(\mathbf{r},\mathbf{r}')\cdot\mathbf{w}(\mathbf{r}')\cdot dV = E_k^{bg}(\mathbf{r}) = 0 \quad (13)$$

where G^{EJ} is the 'electric current to electric field' Green's tensor. The tissue parameters are found by iterative minimization of the function F given by the sum of the 'data equation' and 'object equation':

$$F(\mathbf{w},\chi) = F_{data}(\mathbf{w}) + F_{object}(\mathbf{w},\chi) \quad (14)$$

By performing this over the whole spatial domain for each $\mathbf{r}$, a coupled set of non-linear equations is obtained relating unknown $\mathbf{w}(\mathbf{r})$, $\chi(\mathbf{r})$ and $\mathbf{E}(\mathbf{r})$. This set is solved in CSI by a so-called alternating update direction gradient search algorithm (see thorough description in Balidemaj et al[45] and van den Berg and Kleinman[49]). Examples of results of CSI-EPT for an abdominal simulation study are given in Figure 1.

In Balidemaj et al,[45] CSI-EPT is only demonstrated *in silico* for a two-dimensional case assuming *E*-polarized waves, where only a transverse magnetic field exists that can be related to the longitudinal electric field E_z. This *E*-polarized field was generated by a set of two-dimensional line sources mimicking the field orientations in the midplane of a birdcage volume. The results showed the capability of the method to reconstruct EP maps free of boundary effects for a heterogeneous human pelvis. The elimination of differentiation and employment of integration including regularization on total variation makes the methodology fairly robust against noise superimposed on the measured H^+ fields. In addition, the simultaneously obtained electric field allows (together with conductivity) the estimation of local SAR.

Interestingly, CSI was originally developed for oil exploration purposes,[50] and later for the mapping of tissue properties,[51] where a 2.33-GHz circular microwave scanner was used. These types of inverse problems are typically ill-posed as there are only a few EM field recordings available from outside the object of interest. The key advantage of EPT using MRI is that EM field information is available *inside* the tested object and thus is more strongly correlated to the dielectric composition of the object. Furthermore, the information available for the reconstruction algorithm is one order of magnitude larger than in conventional CSI with recordings in the far field of the scattering object with an array of EM field sensors.

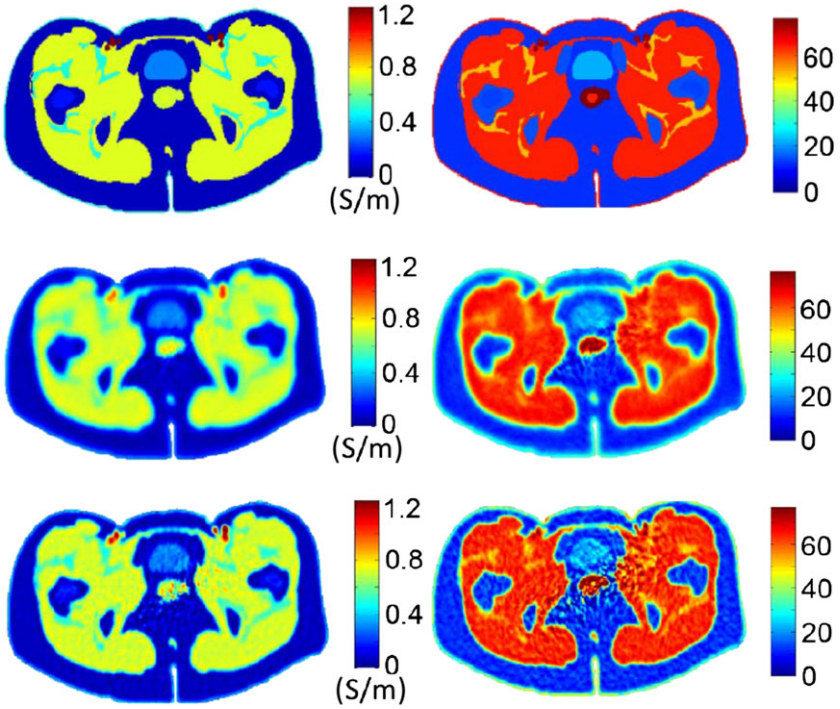

FIGURE 1 Top row: Input conductivity (left) and permittivity (right) maps employed to compute the B_1^+ field at 128 MHz used for contrast source inversion-electrical properties tomography (CSI-EPT) reconstructions. Additive Gaussian noise [signal-to-noise ratio (SNR) = 20] was added to the three B_1^+ maps generated using two linearly and one circularly polarized modes to mitigate the issue of zero electric field regions. Minimization of total variation was employed to mitigate noise. Two-dimensional *in silico* CSI-EPT reconstructions of conductivity and permittivity after 1000 iterations (middle row) and after 5000 iterations (bottom row). Reprinted from PhD thesis of (E. Balidemaj, PhD thesis: MR based electric properties imaging for hyperthermia treatment planning and MR safety purposes, Digital Academic Repository, University of Amsterdam, 2016, ISBN 978–94–028-0165-1)

After the introduction of CSI, the concept of solving EPT as a forward problem was picked up by further groups. A direct inversion of Poisson's equation (Equation 8), combined with various types of regularization, has been presented.[46,47] In Serralles et al,[48] the above-mentioned LMT[43,44] was converted to a forward problem, now called 'global Maxwell tomography'. Based on Song and Seo,[52] Ammari[53] iteratively minimized the mismatch between the forward model and observed data starting with an initial guess by solving Equation 11 for the complex H^+. This method was further developed by Palamodov.[54]

4 | NUMERICS

4.1 | Differentiation

The need for spatial differentiation of measured H^+ or H^- field maps plays a central role in EPT reconstruction. As obvious from Equations 6–9, the differentiation of the H^+ amplitude and H^+ phase can be performed separately for the different spatial dimensions. As the H^+ or H^- field data are reconstructed on a finite grid, *direct* differentiation should be performed through a finite difference scheme. This could be a backward, central or forward scheme. Finite difference differentiation schemes are numerical approximations of the true derivative and higher order terms. Backward and forward finite differentiation have first-order truncation errors, i.e. ignore terms of order Δx (voxel size for an isotropic grid). A central finite difference scheme has a lower truncation error and is accurate up to the order of Δx^3. However, most EPT studies do not employ direct finite difference differentiation, but use so-called Savitzky–Golay convolution.[55] This methodology is more robust to noise present in the data. The method is based on an analytical solution to a least-squares fitting of a polynomial of order n to m local data points around the point of consideration. In this way, first- and second-order differentiation can be performed analytically on the fitted polynomial. The final result is that derivatives can be written as a kernel, i.e. a linear combination of data values of the kernel points with particular weights depending on the order of the derivation, the order of the fitted polynomial and the size of the kernel, i.e. the number of neighboring data points taken into account. Tables providing the weights given the order of the differentiation and polynomial have been published.[56] The noise mitigation effect of Savitzky–Golay-based differentiation over the finite difference schemes arises from the polynomial fitting of the data point.

To further mitigate noise in the H^+ field data, often large kernels are applied in practice. This works provided that the dielectric contrast only contains low spatial frequencies. Looking, for instance, at the human brain, this is, however, certainly not the case. Thus, at tissue boundaries, the approximation for the *local* derivate is corrupted as H^+ field data are included in the kernel from the neighboring tissue compartment with differing EPs. This typically leads to under- and overshooting of the reconstructed conductivity and permittivity values at the boundaries. The spatial extent of these erroneous regions can be decreased by reducing the differentiation kernel (see Figure 2 for an illustration of this effect on simulated H^+ data of a phantom consisting of various conductivity compartments). In practice, smaller kernels quickly lead to an increased sensitivity to noise. This latter aspect is often more pressing, and therefore relatively large kernels of five or seven points are typically used for second-order differentiation in EPT. It should be noted that this 'derivative'-related boundary effect is independent of the invalidity of the Helmholtz equation at the boundary and its resulting boundary errors.

Recently, a study has been published that has investigated the impact of different differentiation kernels.[58] In this work, expressions were derived for the precision of the reconstructed EPs based on the SNR of the H^+ magnitude and phase. In this analysis, the authors also

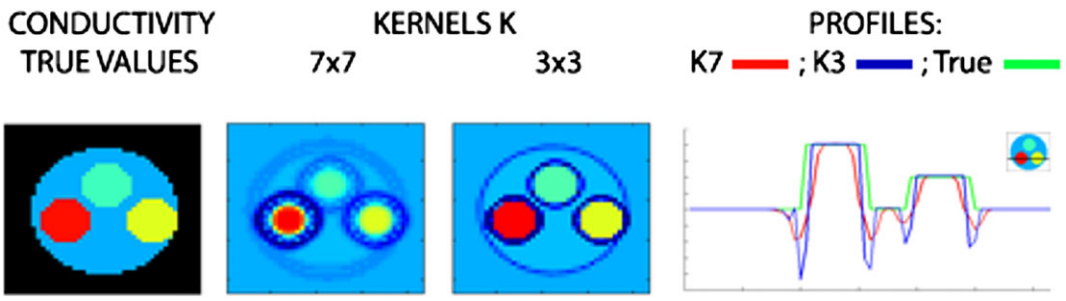

FIGURE 2 Illustration of the impact of different differentiation kernels on the amplitude and extent of the boundary effects (noiseless case). Larger kernels lead to lower undershooting, but increased spatial extent of the affected region. Figure taken from Mandija et al[57]

explained the empirically observed improvement[29] in the precision of EPT reconstructions for higher field strengths, as the uncertainty was shown to be inversely proportional to the imaginary and real part, respectively, of the squared complex wavenumber κ^2, and thus to the RF frequency and B_0.

4.2 | Denoising filters

Noise amplification is an intrinsic problem of EPT, independent of the reconstruction algorithm chosen. As a result of the intrinsic nature of this noise problem, denoising filters to counteract this problem should not be considered as cosmetic operations to improve some awkward image appearance, but as an inevitable, additional reconstruction step. Indeed, all EPT studies published so far (except for those on noise-free synthetic data) have applied denoising filters in one way or another. Denoising filters can be applied: (i) before the differentiation step (i.e. on the B_1 map); (ii) after the differentiation step (i.e. on the 'raw' conductivity map); or (iii) in combination with the differentiation step (e.g. by enlarging the differentiation kernel, see previous section). In the case of a linear denoising filter and a linear differentiation algorithm, these three variants (i)–(iii) yield identical results. However, non-linear filters are known to be superior to linear filters with respect to preserving significant (physical/physiological) spatial features, and the order of the non-linear filtering and differentiating steps has an impact on the reconstruction result.

In Seo et al,[33] the B_1 field map was filtered by a Gaussian explicitly (i.e. filtering was not combined with differentiation). In Michel et al,[59] an adaptive non-linear diffusion filter was applied to the B_1 field map, using geometric parameters derived from the signal magnitude to calculate the diffusion coefficients in the different spatial directions. The authors preferred to filter real and imaginary parts of the B_1 map, instead of its magnitude and phase, to ease the interpretation of results.

Bilateral filtering of the noisy 'raw' conductivity maps is illustrated in Figure 3. Bilateral filtering shapes the filter kernel not only with respect to the spatial distance to the target voxel, but also with respect to the 'similarity' to the target voxel. Ideally, the filter kernel should contain only voxels of the same conductivity, i.e. only voxels of the same tissue type. As the noise in the unfiltered 'raw' conductivity is typically much higher than the conductivity difference between tissue types, this kernel shaping cannot be based on the 'raw' conductivity itself. Instead, tissue type is preferably identified by a magnitude image, which is typically the magnitude of the image acquired for transceive phase determination. For instance, the kernel can be limited to voxels with a signal amplitude $A(\mathbf{r})$, which differs from the signal amplitude of the target voxel, $A(\mathbf{r}_{\text{target}})$, by less than a certain threshold R_{thresh}:

σ_1	σ_1	σ_1	σ_1	σ_1	σ_1	σ_1	σ_1	σ_1
σ_1	σ_1	σ_1	σ_1	σ_1	σ_1	σ_1	σ_1	σ_1
σ_1	σ_1	σ_1	σ_1	σ_1	σ_1	σ_1	σ_1	σ_1
σ_1	σ_1	σ_1	σ_1	σ_1	σ_1	σ_1	σ_1	σ_1
σ_1	σ_1	σ_1	σ_1	σ_1	σ_1	σ_1	σ_1	σ_1
σ_1	σ_1	σ_1	σ_1	σ_1	σ_1	σ_1	σ_1	σ_1
σ_1	σ_1	σ_1	σ_1	σ_1	σ_1	σ_1	σ_1	σ_1
σ_1	σ_1	σ_1	σ_1	σ_1	σ_1	σ_1	σ_1	σ_1
σ_1	σ_1	σ_1	σ_1	σ_1	σ_1	σ_1	σ_1	σ_1

σ_2	σ_2	σ_2	σ_2	σ_2	σ_2	σ_2	σ_1	σ_1
σ_2	σ_2	σ_2	σ_1	σ_2	σ_2	σ_2	σ_2	σ_1
σ_2	σ_2	σ_2	σ_1	σ_2	σ_2	σ_2	σ_2	σ_2
σ_2	σ_2	σ_2	σ_1	σ_1	σ_1	σ_2	σ_2	σ_1
σ_2	σ_2	σ_2	σ_1	σ_1	σ_1	σ_1	σ_1	σ_1
σ_2	σ_2	σ_2	σ_1	σ_1	σ_1	σ_1	σ_1	σ_1
σ_2	σ_1	σ_1	σ_1	σ_1	σ_1	σ_1	σ_1	σ_1
σ_2	σ_1	σ_1	σ_1	σ_1	σ_1	σ_1	σ_1	σ_1
σ_2	σ_1	σ_1	σ_1	σ_1	σ_1	σ_1	σ_1	σ_1

FIGURE 3 Illustration of bilateral filtering in two spatial dimensions. Left: In a homogeneous tissue with conductivity σ_1, the filter kernel (orange voxels) around the target voxel (green) has its predefined maximum size (here, 5 × 5 voxels). Right: At the boundary between two tissues (having yellow and blue conductivities σ_1 and σ_2, respectively), the filter kernel is restricted to voxels having the same conductivity, i.e. belonging to the same tissue type. Typically, tissue type is identified from an independent magnitude image

$$R(\mathbf{r}) = \left|A(\mathbf{r})/A(\mathbf{r}_{\text{target}})-1\right| < R_{\text{thresh}} \quad (15)$$

Bilateral filtering was first introduced for EPT by Katscher et al[60] and studied in more detail using a Monte Carlo method.[61] Moreover, it is possible to combine multiple images to suitably shape the kernel. In Katscher et al,[62] a steady-state free precession (SSFP) image was taken to distinguish gray and white matter, and, in addition, a quantitative susceptibility map[1,2] was used to distinguish deep gray matter nuclei, showing sufficient contrast on quantitative susceptibility mapping (QSM) but not on SSFP images.

5 | MR SEQUENCES FOR EPT

Although the magnitude and phase of the TX RF field constitute a complete complex EM field component, separate MRI sequences and techniques are required to map them. Although the equations above are formulated for the magnetic field H^+, it is standard in MR literature to use the magnetic flux density B_1 instead. As, for EPT, any scaling of the TX RF field is irrelevant, as discussed above, this article tantamounts H^+ and B_1.

The TX magnitude $|H^+|$, required for EPT, can be measured in a straightforward manner because of its non-linear impact on the MR signal. Numerous techniques for $|H^+|$ mapping (B_1 mapping) have been published (see, for example, previous studies[15-18]). In principle, EPT can be based on any B_1 mapping method. The accuracy of EPT depends on the accuracy of this mapping, i.e. the most accurate B_1 mapping method leads to the most accurate EPT results. Studies looking for the optimum B_1 mapping technique, independent of EPT, have been published elsewhere (see, for example, Pohmann and Scheffler[63]).

As discussed in the previous section, determination of the B_1 phase φ^+ always starts with the measurement of the transceive phase. One of the main issues of EPT, as already pointed out by Haacke et al,[12] is the decontamination of the transceive phase by unwanted phase contributions unrelated to RF penetration:

1. The image phase must not contain any contributions from B_0, i.e. any off-resonance effects. The easiest way to exclude off-resonance effects is the use of refocusing pulses, i.e. sequences based on spin echoes, such as fast spin echo sequences, turbo spin echo sequences, etc. In contrast, the image phase of field echo (gradient echo)-based sequences includes off-resonance effects. In this case, these effects can be removed by any kind of B_0 mapping. In the simplest way, phase can be measured at two different TEs and extrapolated back to TE = 0. More sophisticated B_0 maps can be applied, e.g. obtained in the framework of Dixon techniques (see, for example, Glover and Schneider[64]). However, sequences with balanced gradients (SSFP) are known to have benign off-resonance behavior. As long as B_0 inhomogeneities are too small to cause the well-known banding artifacts, which lead to phase jumps of 180°, the SSFP image phase fairly resembles the image phase of spin echo sequences.[32]
2. The transceive phase must not contain any contributions from eddy currents induced by gradient switching. This can be obtained by averaging two separate measurements with inverted gradient polarization.[31] Alternatively, the balanced gradients of SSFP sequences essentially eliminate this unwanted phase contribution automatically.[32]
3. Phase contributions from flow and motion should be removed or at least suppressed as much as possible. This can be achieved, for example, by double spin echo sequences[65] or, again, by SSFP.[32]
4. If the 'full' complex EPT equation has to be solved and not the phase-based version of EPT, the transceive phase must be unwrapped before dividing by two (Equation 5). This unwrapping can be facilitated by performing it separately for each spatial dimension, as differentiation is performed separately for each spatial dimension. Alternatively, differentiating the real and imaginary parts of the MR signal instead of its phase supersedes phase unwrapping (see, for example, de Leeuw and Bakker[66]).

EPT cannot be performed correctly on a single two-dimensional image, as the differential operators in Equation 1 (and the following equations derived from Equation 1) work in all three spatial dimensions. Thus, EPT requires a 'true' three-dimensional dataset or multiple two-dimensional datasets. Multiple two-dimensional datasets leading to effective three-dimensional coverage have the advantage of higher robustness in the case of patient motion. However, multiple two-dimensional datasets might suffer from inconsistent sequence calibration between slices, hampering reliable through-plane differentiation. This problem does not occur in true three-dimensional datasets.

Care must be taken if the transceive phase maps of multiple RX coils have to be combined to a single phase map. This general problem has been investigated in the framework of EPT by previous studies.[67,68]

After scanning, the numerical Laplacian operator is usually applied to the obtained B_1 according to Equation 4. Alternatively, a direct (approximate) measurement of the Laplacian can be performed by a suitable k-space sampling scheme, utilizing the T_2 weighting of a spin echo train.[69] Two measurements with inverted sampling schemes per spatial dimension can be used to approximately mimic the frequency response of the Laplacian operator.

The phase contribution from off-resonances in field echo-based sequences evolves linearly with TE, i.e. the shorter the TE, the smaller this unwanted contribution. This feature allows us to base EPT on the transceive phase of sequences with ultrashort or zero TEs (UTE/ZTE),[70,71] and thus to enable EPT for tissue with fast relaxation, such as lung[72] or cartilage.

The impact of B_0 on EPT by a more pronounced EM interaction at higher RF frequencies, and the related question of the optimal B_0 for EPT, turns out to be a non-trivial task.[29] Obviously, higher SNR can be expected with increasing B_0. This advantage is counterbalanced by the increasing violation of the assumption $|H^+|$ = constant for Equation 8 or the QBC transceive phase assumption (Equation 5). Although not explicitly stated by the authors,[29] the optimal tradeoff between SNR and reconstruction

accuracy seems to be given at B_0 = 3 T for conductivity imaging. For permittivity imaging, the violation of the assumption φ^+ = constant does not increase with B_0, and the highest available B_0 seems to be optimal.[29,58] This trend is further emphasized by the squared ω in Equation 9 in contrast with Equation 8.

In principle, phase-based EPT only requires a standard image's transceive phase, which usually comes for free with every MR sequence. It opens up the possibility that conductivity can be obtained via sequences which are not primarily performed for EPT, by just re-using the transceive phase. Thus, it is more or less straightforward to combine phase-based EPT with all kinds of other MRI types, yielding hybrid imaging. Below, some possible combinations are sketched.

EPT has been combined[73,74] with quantitative mapping of the magnetic susceptibility (QSM[1,2]). This combination is driven by the idea to obtain a complete EM description of the tissue. EPT and QSM are based on different components of the transceive phase of a gradient echo image, i.e. the components related to B_1 and B_0, respectively. The separation of these two components, e.g. by extrapolating the phase of a multi-echo sequence to TE = 0 as described above, is the basis of both EPT and QSM. When interested only in EPT or in QSM, the non-interesting part of the phase is just dropped. Thus, the combination of EPT and QSM is simply performed by not dropping one part of the phase, but using both parts as input for the respective approaches.

Another hybrid imaging technique combines EPT with amide proton transfer (APT).[75] By measuring the asymmetry of the magnetization transfer via different RF saturation offset frequencies, APT reflects elevated protein levels, which yields biochemical information complementary to the information obtained with EPT. A technical synergy effect arises from the possibility to perform the different RF saturations with alternating gradient polarization to eliminate eddy current effects as described above.

Yet another fruitful combination is obtained by performing EPT and MR-EIT simultaneously.[33,76] By injecting external currents in the patient for a few milliseconds between RF pulse and signal sampling, MR-EIT is able to extract tissue conductivity related to $\omega \approx$ kHz corresponding to the duration of the current injection. In contrast, conductivity determined with EPT is related to the Larmor (MHz) frequency. Thus, the EPT/MR-EIT hybrid sequence yields a minimal form of conductivity 'spectrum', in which the low-frequency conductivity predominantly reflects the cellular structure/composition of tissue and the high frequency conductivity reflects the ionic and water content of tissue.[77] This frequency dependence can be strikingly proven by wrapping (parts of) phantoms in isolating foil. The EPT result is not at all affected by the wrapping. For MR-EIT, the apparent conductivity of the wrapped part is completely suppressed.[33]

Using a hybrid positron emission tomography (PET)-MR system, fluoro-ethyl-tyrosine (FET)-PET of patients with meningioma was combined with different MR contrasts [fluid-attenuated inversion recovery (FLAIR), magnetization-prepared rapid gradient echo (MPRAGE)] and quantitative physiologic parameters (conductivity, susceptibility and water content) to demonstrate the technical feasibility of this comprehensive, multi-parametric approach.[78]

6 | VALIDATION EXPERIMENTS

6.1 | Phantom studies

The central validation of EPT is to prove the correlation between EPT measurements and the expected EPs of different phantoms. The expected EPs can be obtained, for example, by independent probe measurements or by the analysis of the chemical phantom content (e.g. NaCl for variation of conductivity; alcohol or sugar for variation of permittivity). The resulting correlation is typically very high.[13,14,79,80] Degradation of this correlation by using phase-based/magnitude-based EPT was analysed in detail by Voigt et al.[30] For phase-based conductivity imaging, an accuracy of 55 mg NaCl/L H_2O (i.e. around 1 mmol/L) can be easily achieved at B_0 = 3 T for phantoms (see Figure 4).

Conductivity is determined not only by the concentration of ions, as demonstrated by the above listed studies, but also by the mobility of ions. This aspect was confirmed by comparing phantoms with identical ion concentration, but different ion size.[81]

EPs of a given substance or tissue depend not only on frequency, but also on temperature. The dependence is roughly +2%/°C for conductivity and −0.5%/°C for permittivity. The temperature dependence of conductivity has been confirmed by EPT.[82] According to this study, temperature dependence is independent of the biologic substance investigated.

In full electrodynamics, EPs are described by a tensor, i.e. EPs can vary between different spatial directions. Such anisotropic behavior is expected for tissue with anisotropic cell structure, such as muscle or nerve/brain tissue structured as fibers. The effect is expected to be dominant at low frequencies, and of decreasing importance with increasing frequencies. For instance, the literature reports no more than a 10% difference in conductivity along and across muscle fibers at typical Larmor frequencies.[83] Nevertheless, attempts have been published to investigate the anisotropic conductivity with EPT.[84,85]

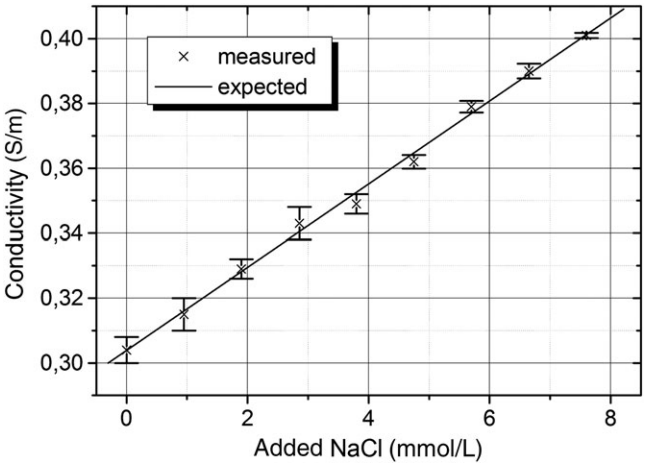

FIGURE 4 Electrical properties tomography (EPT) phantom measurements at different saline concentrations. The plot clearly shows the different steps of added NaCl, corresponding to an accuracy of about 10 mS/m. Error bars indicate standard deviation over the averaged 50 × 50 voxels in the center of the phantom

6.2 | *In vivo* studies

The next level of validation is given by volunteer studies for different healthy target organs, such as brain,[30] breast,[86] liver,[87] muscle and bladder.[88] An example of a brain conductivity reconstruction of a healthy volunteer is given in Figure 5. The obtained EPs are always in the range expected from literature values (see, for example, Gabriel et al[89]). The observed intra-subject variability is typically around 10%. As system imperfections of this order of magnitude can be excluded from corresponding phantom reproducibility experiments (typically yielding a variability below 1%), the intra-subject variability obviously arises from physiology-induced B_1 disturbances, even in adjacently repeated scans. A potential impact of the volunteer's status (e.g. nutrition) has not yet been investigated, except for a single-case stomach study.[32] The reported inter-subject variability is typically only slightly higher than the intra-subject variability, i.e. the main differences between subjects are obviously caused by basic physiologic scan disturbances.

A further validation of EPT was performed by Tha et al.[90] Here, phase-based conductivity imaging of *in vivo* brain tumors was compared with independent probe measurements of the conductivity of corresponding excised tumor samples. The correlation obtained was around 75%. A similar validation has been reported within the framework of a xenograft rat tumor model.[91]

7 | PHYSIOLOGIC BACKGROUND OF ELECTRICAL TISSUE PROPERTIES

To assess the potential value of RF conductivity or permittivity as a biomarker, it is important to understand the relationship between EPs and tissue structure and composition. Electrical probe measurements for a large number of tissue types have demonstrated that the human body is dielectrically very heterogeneous and tissue EPs vary strongly with frequency. In this respect, it is worth mentioning the work of Gabriel et al,[83,89,92] whose values are largely used in EM modeling studies on electromagnetic field (EMF) exposure.

To understand these findings, researchers have taken a modeling approach. A first simple phenomenological model of tissue was introduced by Fricke,[93] describing the EPs of densely packed cells as conducting spheroids (cytoplasm) surrounded by a non-conducting layer (the cell membrane) immersed in an electrolyte (extracellular space). These types of phenomenological models that describe EPs of multi-phase media in terms of the properties of the separate constituents (e.g. volume fractions, single-phase EPs) are typically denoted by effective medium theories or Maxwell mixture theory.[77]

Schwan[94] expanded the work of Fricke[93] and developed a more elaborate mixture model by adding a resistance to the cell membrane. He demonstrated that the capacitance of cell membranes is relatively independent of frequency. He found a capacitance C of 1 μF/cm^2, which was later reproduced for organelles, bacteria and other living cells. This is probably a result of the similar composition of membranes consisting of lipid bilayers. The resistance R is more difficult to assess, but commonly accepted values vary around 0.1–1 Ω cm^2.[95] This leads to a frequency-dependent total membrane impedance:

$$|Z| = \frac{1}{\sqrt{\left((1/R)^2 + (\omega \cdot C)^2\right.}} \tag{16}$$

This membrane impedance is most strongly modulated in the 100 kHz to 10 MHz range, the so-called β dispersion of tissue, where capacitive charging effects of the membrane are prominent. This leads to a relatively strong variation of conductivity, as well as permittivity, in this frequency band. Around 100 MHz, the impedance of the membranes becomes so small that RF currents are no longer hindered by the cell membrane. Thus, the EPs become largely independent of the cell membranes.[95] Above 100 MHz, the EPs of tissue can be described by Maxwell mixture theory,[77] modeling tissue as low-conductivity/permittivity particles (cells) immersed in an aqueous electrolyte solution (extracellular space). Schwan and Foster[96] concluded that, at microwave frequencies, the EPs of tissue can be modeled in terms of ionic and water content. Recently, this finding was revived by Michel et al,[97] introducing water content-based EPT ('wEPT'). In this work, the authors employed a previously published relationship between water content and longitudinal relaxation time T_1 to derive the water content from a series of MR images.[98] Subsequently, water content images were transformed into permittivity and conductivity images using empirical relationships computed from the literature and validated with phantoms. Thus, the methodology employs a double calibration, i.e. it assumes a fixed relationship between longitudinal relaxation and water content, on the one hand, and a fixed relationship between water content and EPs on the other. Whether these relationships hold for a large population remains to be demonstrated and, as the authors outline, pathologies such as tumors might be characterized by other relationships between water content and EPs. Nevertheless,

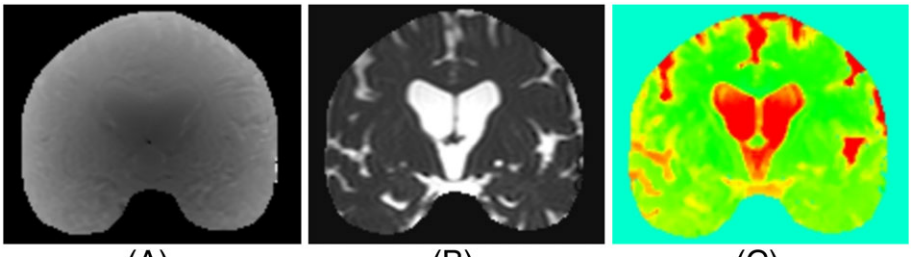

FIGURE 5 Example of a brain conductivity reconstruction of a healthy volunteer [phase-based electrical properties tomography (EPT)]. A, phase image of a steady-state free precession (SSFP) scan used for differentiation. B, magnitude image of an SSFP scan used for boundary detection to avoid boundary artifacts. C, reconstructed conductivity

the methodology has clear merits over conventional EPT, being free from the discussed boundary effects and the ability to map EPs at relatively high spatial resolution. The study was performed at 3 T, i.e. employing an RF outside β dispersion, where a clear relationship between water content and EP is expected based on the aforementioned theory. It might be interesting to perform a similar study at 1.5 T with a simultaneous validation by standard EPT. In addition to the water content, a clear relationship between conductivity and ionic content is also anticipated. Preliminary investigations at 7 T[99] using sodium imaging and EPT have found strong indications for the existence of a linear relationship between Na^+ content and conductivity. In general, Maxwell mixture theory predicts a direct relationship between conductivity, on the one hand, and ionic and water content, on the other, for frequencies larger than 100 MHz. The ability of MRI to perform sodium imaging, probing the dominant electrolyte (Na^+) in human tissue, in addition to T_1-based water content and EPT-based conductivity and permittivity, makes MRI an ideal modality to study this relationship.

Although the aforementioned phenomenological models treat tissue as a passive medium, this is, of course, not the case for living tissue. In living tissue, various fundamental biophysical processes regulate ionic homeostasis. The key cellular mechanism is the sodium–potassium pump regulating intra- and extracellular ionic homeostasis. This active mechanism (requiring ATP) transports potassium ions into cells, whilst sodium ions are removed from the cytoplasm. This leads to an intra-cellular sodium concentration of approximately 10 mmol/L, whereas the extracellular sodium concentration is approximately 140 mmol/L (see, for example, Ouwerkerk et al[100] and references therein). This gradient in concentration is used as a source of energy by transport proteins in the cellular membrane that are responsible for the transport of glucose, amino acids and other nutrients into the cells. The pump also regulates the osmolarity of cells, and thus also the transport of water molecules into and out of the cells.

7.1 | Stroke

Ischemic stroke, which deprives the cells of nutrients and oxygen, causes the breakdown of the sodium–potassium pump as ATP is no longer available in sufficient quantities. This leads to increasing levels of intracellular sodium, and hence abnormal ionic homeostasis and cell osmolarity. As a result, water molecules start to enter the cells, leading to abnormal swelling and, finally, to cell membrane rupture and thus cell death. As found by several studies employing sodium imaging for stroke, the total sodium concentration of tissue is increased by this process as intracellular sodium increases, whereas the extracellular sodium concentration, buffered by the human body, is maintained at 140 mmol/L. This suggests that conductivity should be increased in this process. This could provide the physiological rationale for employing EPT in acute stroke imaging, where MRI is the preferred imaging modality. A combination of diffusion-weighted imaging (DWI) and contrast-enhanced imaging is currently used clinically to identify the penumbra tissue region that is hypoperfused, but still viable to regeneration by therapy. After initial enthusiasm, it has become clear that the use of DWI and contrast-enhanced imaging does not always allow the precise discrimination between still viable tissue and irreversibly affected tissue. Recent sodium imaging studies on acute stroke have found increased sodium levels several hours after the onset of stroke.[101-103] The hypothesis is that sodium imaging should be better suited to mark the cut-off between viable and non-viable tissue by the quantification of Na^+ levels. The clear downside of sodium imaging is that it is not readily available in acute situations, requires dedicated hardware and suffers from low sensitivity. EPT, which is feasible by regular MRI systems, could provide an alternative quantitative biomarker that is expected to be linearly related to sodium concentration for frequencies higher than 100 MHz.

7.2 | Cancer

Tumor neovascularization leads to microvasculature that is very inefficient in transporting oxygen and nutrients to the surrounding cells. Especially in the case of large tumors, there will be areas in which cells will be deprived of sufficient ATP required to drive the sodium–potassium pump. As a result, ionic homeostasis will be compromised and, similar to the case of stroke, intracellular sodium of tumor cells will rise, leading to an increase in conductivity.[104-107] In addition, neovascularization and the increase in the interstitial space will result in a higher extracellular volume fraction. The corresponding higher water content will typically cause a further increase in conductivity as well as a higher permittivity.

8 | CLINICAL APPLICATIONS

The issues of boundary treatment, as well as the averaging feature of the numerical differentiation and denoising typically applied, suggest that the predominant strength of EPT is the characterization of volumetric areas. Thus, the investigation of tumors, for example, seems to be more appropriate for the current capabilities of EPT than the investigation of structures such as vessel walls or nerve fibers. Indeed, the first clinical studies performed with EPT were dedicated to tumors.[108,109] Moreover, current EPT studies are focusing on brain and breast tumors (see below), but also on cervical tumors with respect to hyperthermia treatment planning.[80,88]

A study on 20 patients with glioma[110] found that sodium levels in tumors were elevated, on average, by 51% (mean total tumor sodium content of 110 mmol/L) compared with contralateral reference regions. Van Lier et al[109] found, by means of MR-EPT at 7 T, that conductivity was also increased in low- and high-grade gliomas (n = 7 patients). It was found that the non-enhancing regions in the tumors had an average conductivity of 1.2 S/m, whereas the conductivity of the enhancing regions was 0.9 S/m (see Figure 6). This was significantly higher than the values found in normal brain tissue, such as gray matter (0.8 S/m) or white matter (0.4 S/m). This consistently increased tumor conductivity was also reported in other studies.[108,111] Advanced EPT brain tumor studies exhibited the possibility that conductivity might even be able to distinguish different World Health Organization (WHO) grades of glioblastoma,[112] as well as different brain tumor types, such as meningioma and lymphoma.[113]

EPT of breast cancer is driven by the desire to increase the low specificity of MR breast tumor diagnosis. This expectation was

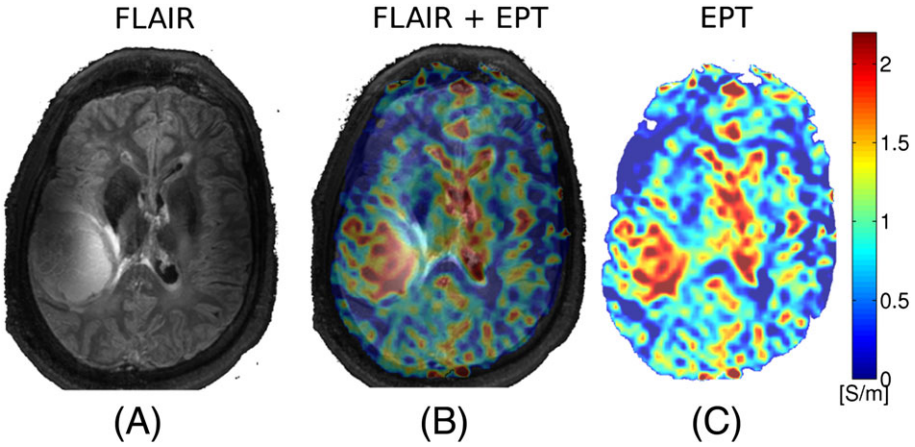

FIGURE 6 Example of grade IV astrocytoma measured at 7 T: A, fluid-attenuated inversion recovery (FLAIR) image; B, FLAIR image overlaid with reconstructed conductivity; C, reconstructed conductivity. Figure taken from van Lier et al[109]

triggered by several *ex vivo*/biopsy studies on the impact of malignancies on EPs. An extensive study by Lazebnik et al[107] performed dielectric characterization in the 0.5–20-GHz frequency range by probe measurements comparing normal and malignant excised breast tissue. In line with previous results,[104-106] they stated that breast cancer tissue had a 40–50% higher permittivity, as well as conductivity, relative to the investigated frequency range of normal tissue. These numbers correspond roughly to the results from sodium imaging,[100] reporting, on average, 63% elevated sodium levels (total sodium content of 53 mmol/L) in malignant tissue compared with normal glandular tissue (34 mmol/L) and normal adipose tissue (16 mmol/L). Importantly, the study by Lazebnik et al[107] also tried to explain the large discrepancies in conductivity ratios of normal and malignant breast tissue reported in various studies. Indeed, if normal breast tissue is considered to be adipose tissue (dominant tissue type in the breast), the ratios are significant and range from 40% to 50%. However, compared with glandular/fibroconnective tissue, which has a relatively high water content, the ratios are reduced to only 10%. Similar findings were obtained by Hancu et al,[114] using probe measurements on mouse models of breast adenocarcinomas and prostate carcinomas, exhibiting a mild increase of 15–20%, with the highest tumor conductivity being 0.9 S/m. A recent *in vivo* study,[115] with $n = 50$ and performing MR-EPT at 3 T, found, on average, a tumor conductivity of 0.9 S/m. The same group[116] published a larger study ($n = 65$) in which, for sufficiently large tumors (>2 cm), they demonstrated that tumors with high mitosis or progesterone receptor (PR) positivity showed higher conductivity than those without, and high mitosis and PR positivity were independently associated with conductivity. Moreover, in Katscher et al[117], MR-EPT revealed a correlation between breast tumor conductivity and malignancy.

The study by Hancu et al[114] also investigated the added diagnostic value of EPT-based conductivity and permittivity mapping *versus* DWI. Based on mouse models, it was essentially concluded that conductivity mapping offers comparable discriminatory power to DWI to separate cancer from normal tissue. Thus, the mapping of both diffusion and conductivity does not outperform the measurement of diffusion of conductivity alone. It is worth mentioning that this finding is not related to physics, but to physiology, as demonstrated experimentally via a combined diffusion/conductivity phantom.[118] It was found that diffusion and conductivity are physically independent parameters; thus, any relationships between diffusion and conductivity found *in vivo* seem to be ascribed by constraining cellular structures.

A few single-case EPT studies of stroke in humans and mice have been described, but with inconsistent findings: in some studies,[119-121] an *increased* conductivity in the affected area was reported, but, in another,[122] a *decreased* conductivity in the affected area was found. This contradiction could be explained by the different time intervals between infarction and EPT measurements in the different studies.

A single-case EPT study of a patient with multiple sclerosis (MS) reported an elevated conductivity rim around an MS lesion.[120]

Two isolated, perfused pig hearts were scanned with a gated SSFP sequence, and conductivity was reconstructed in normally perfused heart muscle and in ischemic regions after blocking the left anterior descending artery.[123] The results for healthy myocardial tissue conductivity were found to be in agreement with the literature.[89] However, conductivity in ischemic/infarcted areas was found to be 60% lower than in healthy myocardial tissue, which is not in line with previous findings, which showed a slight increase in conductivity in ischemic/infarcted areas.[124]

9 | CONCLUSION/OUTLOOK

Post-processing of measured complex B_1 maps allows the quantitative determination of conductivity and permittivity *in vivo* using standard MR systems and standard MR sequences. This represents a crucial difference from previous attempts to measure electrical tissue properties, thus elevating electrical tissue properties to the group of endogenous biomarkers which can be handled routinely in the clinic. Extensive investigations into the field of electrical tissue properties, which died out roughly 50 years ago because of a lack of suitable measurement techniques, will be revived by this readily available method.

The basic problem of EPT is essentially simple and well-posed. However, it is challenged technically by the separation of TX and RX RF phases, as well as the treatment of spatially varying EPs, particularly at tissue boundaries. Both challenges are the subject of numerous

research studies, and are expected to be solved by certain pragmatic workarounds, or by new, alternative reconstruction concepts principally avoiding these challenges.

However, EPT is not confronted only by reconstruction challenges. The 'spurious phase effects unrelated to RF penetration', which hindered Haacke et al[12] in the performance of EPT in the 1990s, are still a major issue for EPT measurements. Phase measurements are extremely sensitive to all kinds of technical and physiologic impact factors, which, on the one hand, represent a welcome feature of MR, but, on the other, open up the door for numerous artifacts, 'which make a simple extraction difficult'.[12] A thorough investigation of these impact factors is required to increase the stability and reliability of RF phase measurements, and thus EPT reconstruction results.

A boost for EPT applications is expected from a clear understanding of the physiologic background of electrical tissue properties, which would link measured electrical tissue properties to the local physiologic situation, and thus a diagnostic interpretation of the findings. Studies have suggested a connection between conductivity (at the Larmor frequency) and the concentration of sodium. If it is shown that these two quantities are physiologically identical, it would be necessary to clarify which of the two methods is superior with respect to accuracy, noise and required hardware, and it is not unlikely that, in these respects, conductivity imaging will outperform sodium imaging. However, it seems more likely that the results of conductivity and sodium imaging will be similar only with regard to leading order, but not completely identical. The remaining differences might be of particular interest, indicating deviations from the healthy biochemical situation. A similar relationship might be found between the measurement of EPs via EPT and via the water content of tissue ('wEPT', see above). Again, it seems likely that results will be similar to some extent, and the remaining differences between the two methods might indicate deviations from the healthy situation. Thus, sodium and/or wEPT might serve as normalization for EPT to reveal pathological areas more clearly.

EPT includes a rich variety of aspects for further comprehensive technical and scientific investigations, challenging physicians, physicists and mathematicians. These investigations are, of course, worthwhile only in the case of clinical applications benefiting from EPT, which are currently surfacing. Thus, combined studies solving the clinical and technical questions of EPT could lead to the establishment of EPs as beneficial biomarkers.

ACKNOWLEDGEMENTS

The authors acknowledge Astrid van Lier, Edmond Balidemaj, Rob Remis and Stefano Mandija for contributions.

REFERENCES

1. Haacke EM, Liu S, Buch S, Zheng W, Wu D, Ye Y. Quantitative susceptibility mapping: Current status and future directions. *Magn Reson Imaging*. 2015;33:1-25.
2. Wang Y, Liu T. Quantitative susceptibility mapping (QSM): Decoding MRI data for a tissue magnetic biomarker. *Magn Reson Med*. 2015;73:82-101.
3. Holder D. *Electrical Impedance Tomography: Methods, History and Applications*. Bristol: IOP Publishing; 2005.
4. Joy ML, Scott GC, Henkelman RM. In vivo detection of applied electric currents by magnetic resonance imaging. *Magn Reson Imaging*. 1989;7:89-94.
5. Scott GC, Joy MLG, Armstrong RL, Henkelman RM. Measurement of nonuniform current density by magnetic resonance. *IEEE Trans Med Imaging*. 1991;10:362-374.
6. Scott GC, Joy MLG, Armstrong RL, Henkelman RM. RF current density imaging in homogeneous media. *Magn Reson Med*. 1992;28:186-201.
7. Scott GC, Joy MLG, Armstrong RL, Henkelman RM. Rotating frame RF current density imaging. *Magn Reson Med*. 1995;33:355-369.
8. Wang D, DeMonte TP, Ma W, Joy MLG, Nachman AI. Multi-slice radio-frequency current density imaging. *IEEE Trans Med Imaging*. 2009;28:1083-1092.
9. Seo JK, Yoon JR, Woo EJ, Kwon O. Reconstruction of conductivity and current density images using only one component of magnetic field measurements. *IEEE Trans Biomed Eng*. 2003;50:1121-1124.
10. Birgül O, Eyüboğlu BM, Ider YZ. Experimental results for 2D magnetic resonance electrical impedance tomography (MR-EIT) using magnetic flux density in one direction. *Phys Med Biol*. 2003;48:3485-3504.
11. Woo EJ, Seo JK. Magnetic resonance electrical impedance tomography (MREIT) for high-resolution conductivity imaging. *Physiol Meas*. 2008;29:R1-R26.
12. Haacke EM, Pepropoulos LS, Nilges EW, Wu DH. Extraction of conductivity and permittivity using magnetic resonance imaging. *Phys Med Biol*. 1991;36:723-734.
13. Wen H. Non-invasive quantitative mapping of conductivity and dielectric distributions using the RF wave propagation effects in high field MRI. *Med Imaging: Phys Med Imaging, Proc SPIE*. 2003; 5030:471-477.
14. Katscher U, Voigt T, Findeklee C, Vernickel P, Nehrke K, Dössel O. Determination of electrical conductivity and local SAR via B1 mapping. *IEEE Trans Med Imaging*. 2009;28:1365-1374.
15. Stollberger R, Wach P. Imaging of the active B1 field in vivo. *Magn Reson Med*. 1996;36:246-251.
16. Yarnykh VL. Actual flip-angle imaging in the pulsed steady state: A method for rapid three-dimensional mapping of the transmitted radiofrequency field. *Magn Reson Med*. 2007;57:192-200.
17. Sacolick LI, Wiesinger F, Hancu I, Vogel MW. B1 mapping by Bloch–Siegert shift. *Magn Reson Med*. 2010;63:1315-1322.
18. Nehrke K, Börnert P. DREAM—A novel approach for robust, ultrafast, multislice B1 mapping. *Magn Reson Med*. 2012;68:1517-1526.
19. Özparlak L, Ider YZ. Induced current magnetic resonance-electrical impedance tomography. *Physiol Meas*. 2005;26:S289-S305.
20. Liu Y, Zhu S, He B. Induced current magnetic resonance electrical impedance tomography of brain tissues based on the J-substitution algorithm: A simulation study. *Phys Med Biol*. 2009;54:4561-4573.
21. De Geeter N, Crevecoeur G, Dupré L. Low-parametric induced current – Magnetic resonance electrical impedance tomography for quantitative conductivity estimation of brain tissues using a priori information: A simulation study. *Proceedings IEEE Eng Med Biol Soc*, Buenos Aires, Argentina, 2010; 5669.
22. van Lier ALH, van den Berg CAT, Katscher U. Measuring electrical conductivity at low frequency using the eddy currents induced by the imaging gradients. *Proceedings of the 20th Annual Meeting ISMRM*, Melbourne, Australia, 2012; 3467.
23. Gibbs E, Liu C. Feasibility of imaging tissue electrical conductivity by switching field gradients with MRI. *Tomography*. 2015;1:125-135.
24. Su J, Zheng B, Li SFY, Huang SY. Further study of the effects of a time-varying gradient field on phase maps – Theory and experiments. *Proceedings of the 23rd Annual Meeting ISMRM*, Toronto, ON, Canada, 2015; 3291.

25. Mandija S, van Lier AL, Katscher U, et al. A geometrical shift results in erroneous appearance of low frequency tissue eddy current induced phase maps. *Magn Reson Med*. 2016;76:905-912.
26. Oran OF, Ider YZ. Feasibility of conductivity imaging using subject eddy currents induced by switching of MRI gradients. *Magn Reson Med*. 2017;77:1926-1937.
27. Hoult DI. The principle of reciprocity in signal strength calculations—A mathematical guide. *Conc Magn Reson*. 2000;12:173-187.
28. Lee SK, Bulumulla SB, Dixon WT, Yeo DTB. B1+ phase mapping for MR-based electrical property measurement of a symmetric phantom. *Proceedings of* the *1st International Workshop on MR-based Impedance Imaging*, Seoul, South Korea, 2011; 54.
29. van Lier ALH, Raaijmakers A, Voigt T, Lagendijk JJ, Katscher U, van den Berg CAT. Electric properties tomography in the human brain at 1.5, 3, and 7 T: A comparison study. *Magn Reson Med*. 2014;71:354-363.
30. Voigt T, Katscher U, Dössel O. Quantitative conductivity and permittivity imaging of the human brain using electric properties tomography. *Magn Reson Med*. 2011;66:456-466.
31. van Lier ALH, Brunner DO, Pruessmann KP, et al. B1 phase mapping at 7T and its application for in vivo electrical conductivity mapping. *Magn Reson Med*. 2012;67:552-561.
32. Stehning C, Voigt TR, Katscher U. Real-time conductivity mapping using balanced SSFP and phase-based reconstruction. *Proceedings of the 19th Annual Meeting ISMRM*, Montreal, QC, Canada, 2011; 128.
33. Seo JK, Kim MO, Lee J, et al. Error analysis of non-constant admittivity for MR-based electric property imaging. *IEEE Trans Med Imaging*. 2012;31:430-437.
34. Duan S, Xu C, Deng G, Wang J, Liu F, Xin SX. Quantitative analysis of the reconstruction errors of the currently popular algorithm of magnetic resonance electrical property tomography at the interfaces of adjacent tissues. *NMR Biomed*. 2016;29:744-750.
35. Liu J, Zhang X, Schmitter S, van de Moortele PF, He B. Gradient-based electrical properties tomography (gEPT): A robust method for mapping electrical properties of biological tissues in vivo using magnetic resonance imaging. *Magn Reson Med*. 2015;74:634-646.
36. Hafalir FS, Oran OM, Gurler N, Ider YZ. Convection-reaction equation based magnetic resonance electrical properties tomography (cr-MREPT). *IEEE Trans Med Imaging*. 2014;33:777-793.
37. Gurler N, Ider YZ. Gradient-based electrical conductivity imaging using MR phase. *Magn Reson Med*. 2017;77:137-150.
38. Zhang X, Van de Moortele PF, Schmitter S, He B. Complex B1 mapping and electrical properties imaging of the human brain using a 16-channel transceiver coil at 7T. *Magn Reson Med*. 2013;69:1285-1296.
39. Zhang X, Zhu S, He B. Imaging electric properties of biological tissues by RF field mapping in MRI. *IEEE Trans Med Imaging*. 2010;29:474-481.
40. Katscher U, Findeklee C, Voigt T. B1-based specific energy absorption rate determination for nonquadrature radiofrequency excitation. *Magn Reson Med*. 2012;68:1911-1918.
41. Liu J, Zhang X, Van de Moortele PF, Schmitter S, He B. Determining electrical properties based on B1 fields measured in an MR scanner using a multi-channel transmit/receive coil: A general approach. *Phys Med Biol*. 2013;58:4395-4408.
42. Marques JP, Sodickson DK, Ipek O, Collins CM, Gruetter R. Single acquisition electrical property mapping based on relative coil sensitivities: A proof-of-concept demonstration. *Magn Reson Med*. 2015;74:185-195.
43. Sodickson DK, Alon L, Deniz CM, et al. Local Maxwell tomography using transmit–receive coil arrays for contact-free mapping of tissue electrical properties and determination of absolute RF phase. *Proceedings of the 20th Annual Meeting ISMRM*, Melbourne, Australia, 2012; 387.
44. Sodickson DK, Alon L, Deniz CM, et al. Generalized Maxwell tomography for mapping of electrical property gradients and tensors. *Proceedings of the 21st Annual Meeting ISMRM*, Salt Lake City, UT, USA, 2013; 4175.
45. Balidemaj E, van den Berg CA, Trinks J, et al. CSI-EPT: A contrast source inversion approach for improved MRI-based EPT. *IEEE Trans Med Imaging*. 2015;34:1788-1796.
46. Ropella KM, Noll DC. A regularized model-based approach to phase-based conductivity mapping. *Magn Reson Med*. 2016.
47. Borsic A, Perreard I, Mahara A, Halter RJ. An inverse problems approach to MR-EPT image reconstruction. *IEEE Trans Med Imaging*. 2016;35:244-256.
48. Serralles JEC, Polimeridis A, Vaidya MV, et al. Global Maxwell tomography: A novel technique for electrical properties mapping without symmetry assumptions or edge artifacts. *Proceedings of the 24th Annual Meeting ISMRM*, Singapore, 2016; 2993.
49. van den Berg PM, Kleinman RE. Contrast source inversion method: State of art. *J Electromagn Waves Appl*. 2001;15:1503-1505.
50. Abubakar A, van den Berg PM. Three-dimensional nonlinear inversion in cross-well electrode logging. *Radio Sci*. 1998;33:989-1004.
51. Abubakar A, van den Berg PM, Mallorqui JJ. Imaging of biomedical data using a multiplicative regularized contrast source inversion method. *IEEE Trans Microw Theory Tech*. 2002;50:1761-1777.
52. Song Y, Seo JK. Conductivity and permittivity image reconstruction at the Larmor frequency using MRI. *SIAM J Appl Math*. 2013;73:2262-2280.
53. Ammari H, Kwon H, Lee Y, Kang K, Seo JK. MR-based reconstruction method of conductivity and permittivity distributions at the Larmor frequency. *Inv Problems*. 2015;31:1-24.
54. Palamodov V. An analytic method for the inverse problem of MREPT. *Inv Probl*. 2016;32:1-5.
55. Savitzky A, Golay MJE. Smoothing and differentiation of data by simplified least squares procedures. *Anal Chem*. 1964;36:1627-1639.
56. Steinier J, Termonia Y, Deltour J. Smoothing and differentiation of data by simplified least square procedure. *Anal Chem*. 1972;44:1906-1909.
57. Mandija S, Sbrizzi A, van Lier ALHMW, Luijten P, van den Berg CAT. Artifacts affecting derivative of B1+ maps for EPT reconstructions. *Proceedings of the 24th Annual Meeting ISMRM*, Singapore, 2016; 2989.
58. Lee SK, Bulumulla S, Hancu I. Theoretical investigation of random noise-limited signal-to-noise ratio in MR-based electrical properties tomography. *IEEE Trans Med Imaging*. 2015;34:2220-2232.
59. Michel E, Hernandez D, Cho MH, Lee SY. Denoising of B_1^+ field maps for noise-robust image reconstruction in electrical properties tomography. *Med Phys*. 2014;41:1-9.
60. Katscher U, Djamshidi K, Voigt T. Estimation of breast tumor conductivity using parabolic phase fitting. *Proceedings of the 20th Annual Meeting ISMRM*, Montreal, QC, Canada, 2012; 3482.
61. Huang L, Schweser F, Herrmann KH, Krämer M, Deistung A, Reichenbach JR. A Monte Carlo method for overcoming the edge artifacts in MRI-based electrical conductivity mapping. *Proceedings of the 22nd Annual Meeting ISMRM*, Milan, Italy, 2014; 3190.
62. Katscher U, Gagiyev M, Meineke J. Conductivity determination of deep gray matter nuclei utilizing susceptibility-based delineation. *Proceedings of the 24th Annual Meeting ISMRM*, Milan, Italy, 2016; 3336.
63. Pohmann R, Scheffler K. A theoretical and experimental comparison of different techniques for B_1 mapping at very high fields. *NMR Biomed*. 2013;26:265-275.
64. Glover GH, Schneider E. Three-point Dixon technique for true water/fat decomposition with B0 inhomogeneity correction. *Magn Reson Med*. 1991;18:371-383.
65. Choi N, Ghim M, Yang S, Zho SY, Kim DH. In vivo conductivity mapping using double spin echo for flow effect removal. *Proceedings of the 19th Annual Meeting ISMRM*, Montreal, QC, Canada, 2011; 4466.
66. de Leeuw HA, Bakker CJG. Correction of gradient echo images for first and second order macroscopic signal dephasing using phase derivative mapping. *Neuroimage*. 2012;60:818-829.

67. Lee JS, Shin JW, Kim DH. MR-based conductivity imaging using multiple receiver coils. *Magn Reson Med*. 2016;76:530-539.
68. Ropella KM, Noll DC. Coil compression for improved phase image signal-to-noise ratio in electrical property tomography. *Proceedings of the 24th Annual Meeting ISMRM*, Singapore, 2016; 1564.
69. Shin JW, Kim MO, Kim JH, Kim DH. Relaxation based conductivity weighted imaging (rCWI). *Proceedings of the 24th Annual Meeting ISMRM*, Singapore, 2016; 1110.
70. Schweser F, Huang L, Herrmann KH, Krämer M, Deistung A, Reichenbach JR. Conductivity mapping using ultrashort echo time (UTE) imaging. *Proceedings of the 21st Annual Meeting ISMRM*, Salt Lake City, UT, USA, 2013; 4190.
71. Lee SK, Bulumulla S, Wiesinger F, Sacolick L, Sun W, Hancu I. Tissue electrical property mapping from zero echo-time magnetic resonance imaging. *IEEE Trans Med Imaging*. 2015;34:541-550.
72. Katscher U, Börnert P. Imaging of lung conductivity using ultrashort echo-time imaging. *Proceedings of the 24th Annual Meeting of ISMRM*, Milan, Italy, 2016; 2923.
73. Kim DH, Choi N, Gho SM, Shin J, Liu C. Simultaneous imaging of in vivo conductivity and susceptibility. *Magn Reson Med*. 2014;71:1144-1150.
74. Gho SM, Shin J, Kim MO, Kim DH. Simultaneous quantitative mapping of conductivity and susceptibility using a double-echo ultrashort echo time sequence: Example using a hematoma evolution study. *Magn Reson Med*. 2016;76:214-221.
75. Doneva M, Katscher U, Stehning C, Togao O, Keupp J. 3D fast spin echo acquisition for combined amide proton transfer and electrical properties tomography. *Proceedings of the 21st Annual Meeting ISMRM*, Salt Lake City, UT, USA, 2013; 4237.
76. Kim HJ, Jeong WC, Sajib SZK, et al. Simultaneous imaging of dual-frequency electrical conductivity using a combination of MREIT and MREPT. *Magn Reson Med*. 2014;71:200-208.
77. Foster KR, Schwan HP. Dielectric properties of tissues and biological materials: A critical review. *Crit Rev Biomed Eng*. 1989;17:25-104.
78. Liao YP, Oros-Peusquens AM, Lindemeyer L et al. Simultaneous water content, electrical conductivity and susceptibility mapping in meningiomas on a 3T MR-PET scanner. *Proceedings of the 24th Annual Meeting ISMRM*, Singapore, 2016; 1563.
79. Katscher U, Karkowski P, Findeklee C, Voigt T. Permittivity determination via phantom and in vivo B1 mapping. *Proceedings of the 18th Annual Meeting ISMRM*, Stockholm, Sweden, 2010; 239.
80. Balidemaj E, Van Lier ALHMW, Crezee J, Nederveen AJ, Stalpers LJA, Van den Berg CAT. Feasibility of electric property tomography of pelvic tumors at 3T. *Magn Reson Med*. 2015;73:1505-1513.
81. Sedlacik J, Katscher U, Fiehler J. Effect of ion size on conductivity measurements of MR-phase-based electric properties tomography. *Proceedings of the 23rd Annual Meeting ISMRM*, Toronto, ON, Canada, 2015; 3294.
82. Leussler C, Karkowski P, Katscher U. Temperature dependent conductivity change using MR based electric properties tomography. *Proceedings of the 20th Annual Meeting ISMRM*, Melbourne, Australia, 2012; 3451.
83. Gabriel S, Lau RW, Gabriel C. The dielectric properties of biological tissues—II. Measurements in the frequency range 10Hz to 20GHz. *Phys Med Biol*. 1996;41:2251-2269.
84. Katscher U, Voigt T, Findeklee C. Estimation of the anisotropy of electric conductivity via B1 mapping. *Proceedings of the 18th Annual Meeting ISMRM*, Stockholm, Sweden, 2010; 2866.
85. Lee J, Song Y, Choi N, Cho S, Seo JK, Kim DH. Noninvasive measurement of conductivity anisotropy at Larmor frequency using MRI. *Comput Math Methods Med*. 2013;42:1619
86. Bulumulla S, Hancu I. Breast permittivity imaging. *Proceedings of the 20th Annual Meeting ISMRM*, Melbourne, Australia, 2012; 2532.
87. Stehning C, Voigt TR, Karkowski P, Katscher U. Electric properties tomography (EPT) of the liver in a single breathhold using SSFP. *Proceedings of the 20th Annual Meeting ISMRM*, Melbourne, Australia, 2012; 386.
88. Balidemaj E, Boer P, Crezee J, et al. In vivo reconstructed conductivity values of cervical cancer patients based on EPT at 3T MRI. *Proceedings of the 23rd Annual Meeting ISMRM*, Toronto, ON, Canada, 2013; 3293.
89. Gabriel C, Gabriel S, Corthout E. The dielectric properties of biological tissues: I. *Literature survey Phys Med Biol*. 1996;41:2231-2249.
90. Tha KK, Katscher U, Yamaguchi S, et al. Electrical conductivity characteristics of glioma: Noninvasive assessment by MRI and its validity. *Proceedings of the 24th Annual Meeting ISMRM*, Singapore, 2016; 274.
91. Liu J, Shao Q, Wang Y, et al. In vivo conductivity imaging of rat tumor model using MRI. *Proceedings of the 24th Annual Meeting ISMRM*, Singapore, 2016; 195.
92. Gabriel S, Lau RW, Gabriel C. The dielectric properties of biological tissues: III. Parametric models for the dielectric spectrum of tissues. *Phys Med Biol*. 1996;41:2271-2293.
93. Fricke H. A mathematical treatment of the electric conductivity and capacity of disperse systems. *Phys Rev*. 1925;26:678-681.
94. Schwan HP. Electrical properties of tissue and cell suspensions. *Adv Biol Med Phys*. 1957;5:147-209.
95. Petig R. Dielectric properties of biological materials: Biophysical and medical applications. *IEEE Trans Elec Insul*. 1984;5:453-471.
96. Schwan HP, Foster KR. Microwave electric properties of tissue: Some comments on the rotational mobility of tissue water. *Biophys J*. 1977;17:193-197.
97. Michel E, Hernandez D, Lee SY. Electrical conductivity and permittivity maps of brain tissues derived from water content based on T1-weighted acquisition. *Magn Reson Med*. 2017;77:1094-1103.
98. Callaghan MF, Helms G, Lutti A, Mohammadi S, Weiskopf N. General linear relaxometry model of R1 using imaging data. *Magn Reson Med*. 2015;73:1309-1314.
99. van Lier ALH, de Bruin PW, Aussenhofer SA, et al. ^{23}Na-MRI and EPT: Are sodium concentration and electrical conductivity at 298 MHz (7T) related? *Proceedings of the 21st Annual Meeting ISMRM*, Salt Lake City, UT, *USA*, 2013; 115.
100. Ouwerkerk R, Jacobs MA, Macura KJ, et al. Elevated tissue sodium concentration in malignant breast lesions detected with non-invasive ^{23}Na MRI. *Breast Cancer Res Treat*. 2007;106:151-160.
101. Hussain MS, Stobbe RW, Bhagat YA, et al. Sodium imaging intensity increases with time after human ischemic stroke. *Ann Neurol*. 2009;66:55-62.
102. Thulborn KR, Gindin TS, Davis D, Erb P. Comprehensive MR imaging protocol for stroke management: Tissue sodium concentration as a measure of tissue viability in nonhuman primate studies and in clinical studies. *Radiology*. 1999;213:156-166.
103. Tsang A, Stobbe RW, Asdaghi N, et al. Relationship between sodium intensity and perfusion deficits in acute ischemic stroke. *J Magn Reson Imaging*. 2011;33:41-47.
104. Chaudhary SS, Mishra RK, Swarup A, Thomas JM. Dielectric properties of normal & malignant human breast tissues at radiowave & microwave frequencies. *Indian Biochem Biophys*. 1984;21:76-79.
105. Surowiec AJ, Stuchly SS, Barr JB, Swarup A. Dielectric properties of breast carcinoma and the surrounding tissues. *IEEE Trans Biomed Eng*. 1988;35:257-263.
106. Joines WT, Zhang Y, Li C, Jirtle RL. The measured electrical properties of normal and malignant human tissues from 50 to 900 MHz. *Med Phys*. 1994;21:547-550.
107. Lazebnik M, Popovic D, McCartney L, et al. A large-scale study of the ultrawideband microwave dielectric properties of normal, benign and malignant breast tissues obtained from cancer surgeries. *Phys Med Biol*. 2007;52:6093-6115.
108. Voigt T, Väterlein O, Stehning C, Katscher U, Fiehler J. In vivo glioma characterization using MR conductivity imaging. *Proceedings of the 19th Annual Meeting ISMRM*, Montreal, QC, Canada, 2011; 127.

109. van Lier ALH, Hoogduin JM, Polders DL, et al. Electrical conductivity imaging of brain tumours. *Proceedings of the 19th Annual Meeting ISMRM*, Montreal, QC, Canada, 2011; 4464.
110. Ouwerkerk R, Bleich KB, Gillen JS, Pomper MG, Bottomley PA. Tissue sodium concentration in human brain tumors as measured with ^{23}Na MR imaging. *Radiology*. 2003;227:529-537.
111. Huhndorf M, Stehning C, Rohr A, Helle M, Katscher U, Jansen O. Systematic brain tumor conductivity study with optimized EPT sequence and reconstruction algorithm. *Proceedings of the 21st Annual Meeting ISMRM*, Salt Lake City, UT, USA, 2013; 3626.
112. Tha KK, Stehning C, Suzuki Y, et al. Noninvasive evaluation of electrical conductivity of the normal brain and brain tumors. *Proceedings of the 22nd Annual Meeting ISMRM*, Milan, Italy, 2014; 1885.
113. Tha KK, Katscher U, Stehning C, et al. Electrical conductivity characteristics of meningiomas: Noninvasive assessment using electric properties tomography. *Proceedings of the 23rd Annual Meeting ISMRM*, Toronto, ON, Canada, 2015; 4397.
114. Hancu I, Roberts JC, Bulumulla S, Lee SK. On conductivity, permittivity, apparent diffusion coefficient, and their usefulness as cancer markers at MRI frequencies. *Magn Reson Med*. 2015; 73:2025-2029.
115. Shin JW, Kim MJ, Lee JS, et al. Initial study on in vivo conductivity mapping of breast cancer using MRI. *J Magn Reson Imaging*. 2015;42:371-378.
116. Kim SY, Shin J, Kim DH, et al. Correlation between conductivity and prognostic factors in invasive breast cancer using magnetic resonance electric properties tomography (MREPT). *Eur Radiol*. 2016; 26:2317-2326.
117. Katscher U, Abe H, Ivancevic MK, Djamshidi K, Karkowski P, Newstead G. Towards the investigation of breast tumor malignancy via electric conductivity measurement. *Proceedings of the 21st Annual Meeting ISMRM*, Salt Lake City, UT, USA, 2013; 3372.
118. Gho SM, Shin JW, Kim MO, et al. Observation of the correlation between electrical conductivity and apparent diffusion coefficient values. *Proceedings of the 24th Annual Meeting ISMRM*, Milan, Italy, 2016; 1566.
119. van Lier ALH, Kolk A, Brundel M, et al. Electrical conductivity in ischemic stroke at 7.0 tesla: A case study. *Proceedings of the 20th Annual Meeting ISMRM*, Melbourne, Australia, 2012; 3484.
120. Huhndorf M, Stehning C, Rohr A, et al. EPT – Measurement of brain conductivity for non-oncologic applications. *Proceedings of the 23rd Annual Meeting ISMRM*, Milan, Italy, 2015; 2194.
121. Gurler N, Oran OM, Keklikoglu HD, Ider YZ. Application of generalized phase based electrical conductivity imaging in the subacute stage of hemorrhagic and ischemic strokes. *Proceedings of the 24th Annual Meeting ISMRM*, Singapore, 2016; 2994.
122. Jensen-Kondering U, Böhm R, Shu L, Katscher U, Jansen O. Electric properties tomography in ischemic stroke: Results of an ex-vivo pilot study. *Proceedings of the 2nd European Stroke Organisation Conference*, Barcelona, Spain, 2016; 270.
123. Voigt T, Schuster A, Ishida M, et al. Conductivity imaging of an ischemic pig heart model using electric properties tomography. *Proceedings of the 20th Annual Meeting ISMRM*, Melbourne, Australia, 2012; 3483.
124. Schaefer M, Gross W, Ackemann J, Gebhard MM. The complex dielectric spectrum of heart tissue during ischemia. *Bioelectrochemistry*. 2002;58:171-180.

How to cite this article: Katscher U, van den Berg CAT. Electric properties tomography: Biochemical, physical and technical background, evaluation and clinical applications. *NMR in Biomedicine*. 2017;0:e3729. https://doi.org/10.1002/nbm.3729